Acta Materialia 56(15), 3990–4001 (2008)

Structure and distribution of oxides in aluminium foam

Alexander Dudka[1,2], Francisco Garcia-Moreno[2,3], Nelia Wanderka[2], John Banhart[2,3]

[1] National Technical University of Ukraine "Kiev Polytechnic Institute", Pr. Peremogy 37, kor. 9, 03056 Kiev, Ukraine

[2] Hahn-Meitner Institute Berlin, Glienicker Strasse 100, 14109 Berlin, Germany

[3] Technical University Berlin, Hardenbergstrasse 36, 10623 Berlin, Germany

Foaming of aluminium is investigated under oxidising and non-oxidising gas atmospheres. Foams were prepared by mixing and pressing Al99.95 and TiH_2 powders and foaming the pressed material in a gas-tight X-ray transparent furnace while following the process by X-ray radioscopy. Structure and distribution of the oxides present in the powders, precursors and foams were studied by light microscopy, scanning and transmission electron microscopy. Sequential focused ion beam slicing was used to obtain tomographic images of oxide and micropore distributions within the individual cell walls of the foams. A complex hierarchical structure of the oxides is found. Oxides reside in the bulk of the cell walls without a pronounced segregation to the gas/metal interfaces. The presence of air retards foaming due to oxidation of the outer surface.

Keywords:

- *aluminium foam*
- *oxide*
- *radioscopy*
- *tomography*
- *TEM*

1 Introduction

Gas nucleated in a metallic melt or injected into a melt gives rise to the formation of bubbles. Provided the melt has been conditioned such that the bubbles are stable and can accumulate, a liquid metallic foam can be produced. After solidification, a solid cellular metallic material is formed that has properties which makes the foam a candidate for, e.g., structural components [1,2].

Metallic foam has been produced in a manifold of different ways. Stable foams always contain a solid constituent dispersed in the melt. The type of solid inclusions, their morphology, shape and distribution depend on the particular system under consideration [3]. For aluminium-based foams made by processing metal powders, the oxides covering the individual powder particles have been recognized to play the most important role for foam stabilisation [4-8]. It is still under dispute how the oxides stabilise the liquid films and prevent them from drying out and rupturing. Mainly two theories are considered: (i) the increase of local viscosity to an extent that the flow of liquid is blocked [3,9] and, (ii) stabilisation of films through oxide agglomerations or networks acting as surface active particles [8] and inducing a particle-based stabilisation mechanism similar to the one proposed for other foaming routes [10,11]. The action of oxides for stabilising foams is mostly discussed indirectly by studying the foamability of precursors containing different oxide contents [12,13]. Reports on direct observation of oxides are rare as they are very thin and difficult to observe. By means of light microscopy and SEM of polished sections [6,8] features which might stabilise foams were identified. Körner et al. [6] postulate that the oxides bunch together to form networks which keep the two gas/metal interfaces of a film apart. This model explains most of the experimental observations including the fact that the metal contained in films is so fluid that films rupture in less than 1 ms according to the latest measurements [14]. In addition to the oxide already present in the powders before compaction, oxides formed during foaming may also play a role. It is known that an oxidising atmosphere has a pronounced effect on the outer skin of metal foams, especially for oxidation-prone aluminium alloys such as Al-Mg, and influences foam expansion [15].

The aim of the present work is to make visible oxide inclusions in the powders, pressed precursors and foams, to identify them as oxides and to determine their crystal type, morphology and structure. We study where oxides preferentially accumulate, near the liquid/gas interface or within the films or Plateau borders of the foams. By foaming under argon and in air we distinguish between oxides present before and formed during foaming. Moreover, we study the influence of the ambient atmosphere on foaming. Very pure

aluminium powder is used since analyses based on commercially pure Al might show phases related to metallic impurities and could lead to misinterpretations.

We apply microscopic tools on different length scales from LOM to SEM, EDX, FIB-tomography and TEM to identify oxide phases. X-ray tomography is used to define the position of the observed oxides within the foam and to obtain an overall picture of the features present in these foams.

2 Experimental

Foamable precursors were manufactured by compacting mixtures of aluminium (Al) and titanium hydride (TiH_2) powder. The aluminium powder used had a nominal purity of 99.95% (metallic impurities) as specified by the manufacturer Chempur (Karlsruhe, Germany). It is most likely air-atomised (not specified) regarding the spattered shape of the individual particles. TiH_2 was purchased from Chemetall (Frankfurt, Germany). The mean particle size of the 'grade N' powder was about 5 μm as specified by the manufacturer, but a d_{50} of 14 μm was found by own analysis. Powders were characterised by using a Sympatec laser diffraction powder analyser to measure the size spectrum and a Horiba carrier gas hot extraction analyser to determine the oxygen content.

Al powder was mixed with 0.5 wt% TiH_2 powder in a tumbling mixer for 15 minutes. The mixture was subjected to uniaxial hot pressing for 5 minutes at 400°C, applying a pressure of 300 MPa. Pressing was carried out in air. Cylindrical tablets (Ø = 36 mm, h = 10 mm) were obtained. Samples of 8×8×2 mm^3 size were cut out of the pressed tablets for the radioscopic measurements.

Foaming was carried out in a X-ray transparent, gas-tight furnace as shown in Figure 1. It consists of an aluminium tube (Ø= 40 mm, l = 200 mm, d = 0.5 mm) sealed at both ends. The furnace can be filled with the required gas, in our case air or argon. The ceramic heating plate on which the samples are foamed has a maximum heating power of 600 W. The sample temperature is measured by a thermocouple which is led through the heating plate and protrudes about 0.5 mm into the foaming sample from below. A PID controller allowed for a pre-defined temperature course: heating up for ≈30 s at maximum heating power, leading to a heating rate of approximately 20 K/s over a wide range for the sample size used, approaching the final temperature of 680°C, and then holding at this temperature for further 70 s. The furnace is described in detail in Ref. [16]. Real-time in-situ X-ray radioscopy during sample foaming was performed with a microfocus X-ray source and a panel detector, both from Hamamatsu. A quantitative expansion analysis of the foams from the radioscopic images in

terms of the cross-sectional expansion A/A_0 was performed with the dedicated software "AXIM" [16].

Tomographic images of the solidified foams were obtained using the same setup as for radioscopy but rotating the samples through 360° in steps of 1° with a rotation stage while acquiring images. From the resulting 360 images a 3D image was calculated using the standard reconstruction software Octopus [17].

For the characterisation of microstructures, unfoamed and foamed samples were embedded in cold-curing resin (Kulzer), mechanically ground with 100 to 2400 grit grinding paper, polished with 3 µm and 1 µm diamonds, followed by final polishing with an oxide suspension (SiO_2) on a soft cloth. In order to enhance visibility of the oxides the surface was etched by the solution of 98% H_2O + 2% NaOH for 5 minutes.

A 3D analysis of the cell wall material was carried out by sequential focussed ion beam (FIB) milling and by imaging the cut cross sections by SEM, both provided by a ZEISS Cross-beam 1540XB. First, the region of interest on the cell wall was chosen, after which a trench was cut as will be shown in Figure 10. 20 nm thick slices were cut from the surface using a 30-kV Ga^+ ion beam and a current of 20 pA. Each slice was SEM-imaged with 7-keV electron energy in the secondary electron mode. This procedure was repeated 172 or 363 times for the two sample positions analysed. For three-dimensional visualisation the images were composed to a 3D image. In addition, energy-dispersive X-ray (EDX) analysis was used to verify the identity of the oxide particles.

The aluminium powders used were analysed to check whether they contained oxides inside the particles, which might have developed during powder atomisation. For this investigation, individual powder particles were sliced by a microtome and were then investigated by transmission electron microscopy (TEM).

TEM specimens from various cell walls in the two foams were prepared as follows: First, 100 µm thick cross-sectional slices were cut from the cell wall with an alumina blade and were mechanically polished down to 5-8 µm thickness using a T-tool technique [18]. After this, they were glued to a molybdenum ring and were Ar^+-ion milled using a BAL-TEC, RES 101 ion mill.

The microstructure of the precursor and of both metal foams was investigated by optical microscopy, scanning electron microscopy (FEI XL30 ESEM and ZEISS 1540XB Cross-Beam) and TEM (Philips CM30).

3 Results

3.1 Powders

The aluminium powder particle size distribution is characterised by d_{50} = 45 μm with 10% < 16 μm, 10% > 85 μm. For the TiH_2 powder, d_{50} = 14 μm with 10% < 3.2 μm, 10% > 31 μm. The oxygen content of the aluminium powder was 0.69±0.04 wt.%. This corresponds to an alumina (Al_2O_3) mass or volume content of 1.46% or 1%, respectively.

3.2 X-ray visualisation of foaming

Figure 2 shows the temperature course and the development of foaming – expressed by the X-ray projected area of the sample – as a function of time for samples foamed under air and argon. The measured temperature profile is close to the ideal profile: a fast heating ramp up to ~680°C at a heating rate of 20 K/s and a constant temperature after. Some oscillations at the beginning of the holding period can be observed, caused by the characteristics of the PID controller. Moreover, melting of the alloy changes the lope of the heating curve. As the measured temperature reading can be influenced by heat directly radiated from the heating plate into the thermocouple and also depends on the position of the tip of the thermocouple inside the foam one should avoid an over-interpretation of individual features of such curves. Different foaming experiments carried out under identical conditions always show a certain scatter in both the temperature and expansion curves.

The quantitative expansion analysis of the radioscopic images shows that after 70 s the cross sectional area A/A_0 for the sample foamed in air falls short of the one foamed in argon. After 100 s the area is about 25% lower in air than under argon which corresponds approximately to a 35% lower volume, since $V \propto A^{3/2}$ for unconstricted uniform foaming. In practice, foaming is not uniform and the interrelationship between V and A is not that simple, which, however, does not affect the interpretation of such curves.

Figure 3 shows radioscopic images of foams after 100 s of heating and foaming both under air (left) and argon (right). The higher expansion of the sample foamed under argon is obvious. Moreover, the sample foamed in air exhibits wrinkly surfaces and dark areas of higher X-ray absorption. The surface of the air-foamed sample is flatter than the argon-foamed one which shows pronounced “surface bubbles”, i.e. bubbles which significantly protrude into the surrounding space.

3.3 Macroscopic foam properties

The surface of the outer skin of the foams made under argon has a yellowish colour, whereas the foam made in air has a darker, greyish colour. The surface of the air-foamed sample is wrinkly, whereas the Ar-foamed sample is smooth.

The resulting foam structures produced in air and under argon atmosphere are shown in X-ray tomographic reconstructions, see Figure 4. Cracked cell walls and interconnections between pores can be observed, see arrows in Figure 4a. They act as channels and connect inner with outer pores. Small holes on the foam surfaces of both samples after solidification can be seen. A closer analysis of the full tomographic data set shows that such holes appear very frequently, up to five times per bubble.

In both the X-ray tomographic and light microscopic cross-sections many cell walls thicker than 250 μm can be found. Thinner cell walls are also present. Cell wall thickness is not uniform but sometimes shows pronounced variations. There is little difference between the foams made under air and argon concerning cell wall thickness.

The oxygen contents of a piece of precursor and of a fragment of a cell wall taken from the foam foamed under argon were both about twice as high as the oxygen content of the powder. The contents in the precursor and in the cell wall were found equal within the statistical error limits of the measurements (usually <0.2 wt.%), each of which is carried out on three individual samples.

3.4 Microstructures

3.4.1 Powders

Figure 5 shows a bright-field TEM image of a specimen prepared from an aluminium powder particle by microtome sectioning. The corresponding selected area electron diffraction (SAED) pattern from the imaged area can be seen in the inset. The annular pattern of SAED indicates a polycrystalline structure. The small dark crystals in the middle of the micrograph contain oxides as verified by EDX analysis (not shown). The individual crystals form a conglomerate of about 1.5 μm size which in turn is embedded in the Al powder particle. SEM images of the sample (not shown) provide evidence of many such oxides inside each individual particle.

3.4.2 Precursors

Figure 6a shows an optical micrograph of a compacted and etched Al + 0.5wt.% TiH_2 precursor. There is a dark contrast in the image around former powder particles which can be

thought to arise from the oxides having covered the particles before compaction and from areas with locally insufficient compaction. Figure 6b and c show particle boundaries in higher magnification. Especially Figure 6c shows that the observed dark features are about 500 nm thick. Metallic bridges with hardly any oxide are also visible (see arrow). There are some traces of oxide located in the interior of the individual particles, but the major part of the oxide particles is distributed around powder particles. Dark phases in some regions between the grains could also be observed which most likely correspond to bi-films formed during powder atomization. Analytical tools such as EDX are needed to actually prove that the dark contrast contains oxygen. We have carried out such analyses as will be demonstrated for the foamed material.

3.4.3 Foams

Figure 7 shows cross sections of films taken from foams produced in air (left side) and under argon atmosphere (right). For each of the foams a film at the outside and in the interior of the foam was chosen. Dark features of different sizes can be seen. We will prove later that these contain aluminium oxide. These features cluster together. Small areas with few oxides are observed. The distribution of oxides depends on the atmosphere during foaming. In air, an approximately 100 μm thick zone containing a lot of oxide is formed on the air side, whereas under argon the oxides are distributed more uniformly. In none of the cases segregation to the gas/metal interface is observed.

The structure of some inner cell walls is shown in Figure 8. These films were selected because they are both thin and show varying thicknesses. Clustering of the oxides is clearly observed in areas of thick films, whereas the regions of the cell walls containing fewer oxides are much thinner.

In order to identify the chemical composition of the features detected by light microscopy, SEM images and corresponding EDX mappings of oxygen and titanium in a film located in the interior of the foams produced under air and under argon atmosphere were made, see Figure 9. The oxide in both specimens (foamed in air and argon) is located preferentially near grain boundaries. A slight oxygen contrast is seen at the surface and within the grains as shown in Figure 9b, but this contrast is too weak to be interpreted as surface segregation. Some small titanium-containing particles (TiH_2) can be seen in Figure 9c (top) as well as one large particle in Figure 9c (bottom).

For a further investigation of the oxide network, a thin area of the cell wall was chosen as shown in the SEM image in Figure 10a. This area is marked by a circle both in Figure 4a

and Figure 10a. Two trenches cut by FIB can be seen in Figure 10b. These were analysed by SEM after. The specimen is tilted in a way that the sequentially cut section of the trench to be analysed can be observed from the top.

Trench I shows areas with different contrast. At the locations marked with '1' to '4' in Figure 10c, EDX analyses were carried out. At positions '1' and '4' an oxygen peak of high intensity was detected besides a peak corresponding to aluminium. The measurements at positions '2' and '3' show mainly aluminium and merely a negligibly small amount of oxygen in the spectra. As expected, a small signal from gallium is also detected because the Ga ion beam used for preparation gives rise to some contamination.

Figure 10d shows a 3-dimensional reconstruction of 172 slices from trench I which were composed to a 6×3.7×1.2 μm^3 large parallelepiped. In this volume oxide conglomerates are visible. The black contrast was found to originate from micropores located inside the inner cell wall as one sees when applying higher magnifications than those used in Figure 10c. The size of such holes ranges up to several hundreds of nanometres and the holes are surrounded by oxide particles.

Trench II yields similar information which is displayed slightly differently here. In the close-up, Figure 10f, of the entire trench section, Figure 10e, grain boundaries and oxide particles can be distinguished. The oxide particles are located at the grain boundaries but there are also grain boundaries which are not decorated with oxides. Figure 10g and 10h represent 3D renderings of the oxide and pore distributions, respectively. On the lower side of Figure 10g and 10h an approximately 2 μm thick pure metallic zone not containing any oxides can be seen. This featureless zone has been omitted from the 3D visualisations in Figure 10g and h. Clearly, oxides and pores are exactly correlated in these visualisations and this correlation is also found in other images. Oxides and pores are very likely to be found very close together.

The oxide microstructure was investigated in more detail using TEM. Elemental mappings using TEM/EDX (not shown) are similar to those measured by SEM/EDX. A bright field TEM image of the specimen foamed in argon is shown in Figure 11a. The corresponding selected area electron diffraction pattern (SAED) associated to this image is given as inset in Figure 11a. Besides the diffraction pattern of the Al matrix, an annular pattern can be seen which arises from many small oxide crystals. The oxide crystal cluster in the middle of the image is polycrystalline as verified by SAED. From the position of the diffraction rings a number of interplanar spacings d_{exp} can be derived. These are given in the Table 1 together with interplanar spacings of known cubic ("γ-alumina" = $Al_{2\frac{2}{3}}O_4$, space group 227 = Fd-3m) and tetragonal ($Al_{10\frac{2}{3}}O_{16}$, space group 141 = $I4_1/amd$) structures of Al_2O_3 [19]. Electron

diffraction yields various values for interplanar spacings which can be explained by assuming that the small crystals are of cubic as well as of tetragonal structure. The oxide agglomerate shown in this image is about 500 nm large. The high-resolution TEM (HRTEM) image in Figure 11b demonstrates the polycrystalline nature of the oxide network. The marked areas show very small crystals between 2 and 8 nm in size, oriented in different directions.

4 Discussion

4.1 Powders

The oxygen content of the air-atomised aluminium *powder*, 0.69±0.04 wt.%, is higher that of the powders used in Refs. [7] and [8], 0.24 and 0.4 wt.%, respectively, and that of the commercial ECKA AS71 powder we used previously for making aluminium-based foams (e.g. in Ref. [20]) for which we determined 0.37±0.03 wt.% oxygen. According to Ref. [12], (result reproduced as Fig. 14 in Ref. [3]) this oxygen content is above the range of optimum foamability. We would therefore expect a low expansion factor, but Figure 2 shows that the observed factors of 4 to 6 indicate very good foaming. We suspect that the calibration of oxygen measurements is a subtle procedure and can lead to systematic errors. We have obtained differing results for the oxygen content of the ECKA AS71 powder in the past (0.7 wt.% in Ref. [21] compared to 0.37 wt.% here), and therefore propose to compare measurements only which were made using the same setup and conditions.

Atomised powders contain oxides not just at the surface but also in the interior, see Figure 5. They form clusters which are some micrometres in size. This is in agreement with the microscopic observations in Ref. [8]. The oxide films covering the surfaces of individual particles are not visible in our images. They are reported to be between 5 and 10 nm thick [22].

4.2 Precursors

In *precursors* (densified powders), surface oxides are clearly discernible at former particle boundaries. These features appear typically 500 nm thick. As the samples were etched to make these features more visible, this might have enlarged the apparent width beyond the actual value. Especially a gap existing between two former particles could be further widened by etching. Sometimes, features looking like double oxide layers (“bi-films”) can be observed, see Figure 6c upper right. Pressing has created metallic contacts between adjacent powder particles and consequently the originally present oxide must have been stripped off under the action of the shearing forces during pressing. The measured oxygen content in the

precursor (and in the foam) is twice as high as in the powder, indicating pickup of oxygen during pressing. Such pickup is possible since the die was not sealed against air during pressing.

4.3 Foams

In *foams* one expects to find oxides since from the literature it is known that the oxide films persist in the melt even after melting and solidification and are then no longer necessarily confined to the former grain boundaries [8]. The arrangement of oxides in the foam (i.e. after melting) is far away from a uniform dispersion of oxides. The cell walls in Figure 7 show both oxides which are not attached to any visible grain boundary and also some oxides which are clearly aligned along a grain boundary. Most likely the latter represent former powder particles which have maintained their integrity even after compaction and foaming. Some of them such as in the upper-right image of Figure 7 even maintain their shape at the metal/gas interface and protrude into the gas phase. The fact that a part of the oxide is still aligned along former powder boundaries is further underlined by SEM images and EDX maps (both in air and argon-foamed samples, latter not shown in Figure 9). Obviously, even during melting of the powder particles some of the oxide pockets persist, allowing the melt to be trapped. Figure 9 also shows the other fractions of the oxide which appears as a cloudy feature and which could represent small oxide particles distributed in the melt.

Some cell walls such as the ones shown in Figure 8 show pronounced thickness variations. Oxides are mainly found in thick sections, whereas low-oxide regions are thin. This fact has been reported by Körner et al. [8]. Segregation of the oxides to the gas/metal interfaces is observed in none of the Figures 7 to 9. Such segregation is known from aluminium foams stabilised with silicon carbide particles [23,24] that modifiy the properties of the gas/metal interface by particle segregation. In contrast, the foams studied in this paper owe their stability to the oxides distributed in the bulk of the cell walls.

FIB tomography shows that the oxide particles bunch together around small – i.e. smaller than 1 µm – pores and form loose conglomerates. The conglomerate analysed in Figure 10d is about 4 µm large. The ‘network particles’ postulated in Ref. [8] could be of this type. Our FIB images do not allow us to decide whether all such oxide conglomerates are connected and form a large network or whether they are separated by layers of pure metal. A 2 µm thick oxide-free zone below the oxide cluster shown in Figure 10g (this oxide-free zone has been cropped) might indicate that oxide clusters do not form a dense network but rather a loose agglomerate. However, without an overview over a larger volume this is difficult to

decide. It is plausible to find pores attached to oxide particles or vice versa since pores can be trapped in conglomerates of oxide particles and the oxide particles can partially de-wet by adhering to the gas/metal interface created by a pore. The almost perfect correlation between pores and oxides seen in Figure 10g and h suggests that pores are already associated with oxides prior to foaming. Precursors of such pores could be created during compaction of the powder by entrapment of gas between individual powder particles. Such entrapped gases would then naturally be adjacent to the surface oxides.

TEM shows that oxides are clustering at an ever smaller scale. Crystallites smaller than 10 nm bunch together to about 500 nm large entities, as seen in Figure 11. The crystal structure determined indicates that the oxide particles found are transition structures which evolve during calcination of $Al(OH)_3$ to the stable α-alumina structure (corundum) in the sequence $Al(OH)_3$→böhmite→γ-alumina→δ-alumina→θ-alumina→α-alumina [25]. γ-alumina forms between 400 and 800°C [26] and can be thought to have originated from hydroxides or böhmite present on the original powder surfaces prior to pressing.

Figure 10f shows that oxides are located at grain boundaries but do not completely enclose the grains. The particle in the middle of this image must have been freely floating in the liquid alloy and must have interrupted the advancing solidification front during cooling. The relationship between oxides and grain boundaries divides the oxides into one of the two types: oxides that are connected to powder particles already before foaming and remain at the grain boundaries after, and oxides that float in the melt and are located at grain boundaries after solidification because these boundaries are formed there. In this context the warning should be given that the situation in the liquid foam might deviate from that in the solid foam after solidification due to pushing effects of the solidification front. At present, an in-situ study which would be needed to assess such effects seems hardly possible.

The oxide conglomerates (or network particles) act in the bulk of the liquid metal film. As such films can be stable for a long time there must be a mechanism preventing the liquid from leaving the thin film, either under the influence of gradients in the Laplace pressure or driven by gravity. One can postulate that the oxides block the channels available for liquid flow in a way that the liquid has to pass such narrow passages that capillary forces holds it in its position. Although the metal is fully liquid, the structure then appears to have an “infinite” viscosity [3]. Alternatively, it has been postulated that rigid network particles modify film curvatures in a way that interface forces hold the liquid in place [8].

Experimentally, it has been shown that once a film ruptures, the liquid is quite volatile [14]. The observed film rupture times around 500 μs allow us to conclude that the viscosity of

the melt is equal to that of the pure liquid metal (≈ 1.5 mPas) within one order of magnitude. In contrast, when trying to explain the observed foam stability in terms of a viscosity increase only, one has to assume apparent viscosities of 400 mPas [9]. The explanation for this apparent contradiction is that the viscosity of a liquid metallic film changes when it is mechanically stressed since the network is disturbed and liquid is allowed to flow. In the same way, viscosity measurements influence the viscosity: using a rheometer, Wübben found that oxide-containing lead melts used to make lead foams merely have 2.5 to 3 times the viscosity of particle-free lead [13], although much higher values would be required to explain foam stability in terms of viscosity. Rheometer measurements therefore do not reflect the situation in a standing metal foam.

These observations suggest that the liquid in a metal film shows a pronounced non-Newtonian behaviour as it is known, e.g. from Bingham or Casson liquids, where a liquid behaves like a solid below a given critical applied shear stress and starts to flow above this threshold [27]. In view of the scarce experimental evidence it is hard to conclude more at the moment.

The kinetics of foaming and the level of maximum expansion are influenced by the atmosphere: in air, expansion is 25% lower than under argon. During foaming in air, a zone of oxidation is created which can be in the order of 100 µm thick at the outside (Figure 7, upper left). This is much thicker than oxide films which grow on solid aluminium surfaces or resting aluminium melts even at high temperatures. This 100 µm thick zone of oxidation is not a homogeneous oxide film but rather a mixture of oxides and metal and could have been created by the movement of the melt caused by foaming during which the liquid film is stretched by bubble expansion. This leads to the constant exposure of fresh metal surfaces to air and prevents the oxide from protecting the liquid alloy. In investigations of dross formation on moving aluminium alloy melts this mechanism has been described [28]. On the inner side of the foams (and of course in argon-foamed foams) no such excessive oxidation occurs since the metal is protected by a hydrogen atmosphere in the liquid state.

The effect of oxygen on foaming has been described in previous studies: Weigand [12] foamed AlSi7 alloys under air, argon and nitrogen and found expansion factors of 7.4, 7.9, 8.1, respectively. The presence of air therefore reduces expansion by 10%. He measured the oxide film thickness on air and argon foamed samples with Auger Electron Spectroscopy (AES) and found values of 92 nm and 30 nm, respectively. Simančík [15] found that oxygen retards foaming of Mg-containing alloys, whereas AlSi10 was hardly affected. Garcia-Moreno [29] studied AlSi6Cu4 and found only a weak effect of air, especially under high

pressure. Pure aluminium was not studied. The samples used in the present study are much smaller than the ones in Refs. [12] and [15]. Therefore, the surface area relative to the volume is larger and a stronger relative influence of the oxide film is expected, explaining the very strong retardation effect of 25% which we observe in air.

As seen in Figure 7, the structure of the surface oxide layer created during foaming is quite complex. The values for the oxide layer thickness provided by AES measurements merely specify the uppermost oxide layer which finally forms after expansion has ended. This most likely uniform layer of alumina is 1000 times thinner than the oxidised zone observed. Another manifestation of oxidation is the different colour, indicating different thicknesses of the oxide layer, and the wrinkly surface of the foam generated in air.

How oxidation hinders foam expansion is not entirely clear. On working hypothesis is to assume that mechanical forces created by the oxide film counteract film stretching. A rough estimate of the order of these forces is: to pull a liquid metallic film of width b apart, a force $F_1 = 2\gamma b$ is required, where γ is the surface tension of the melt. If this film is covered by a solid alumina layer, thickness d_i on the inner side, d_o on the outer, an additional force $F_2 = \sigma b(d_i+d_o)$ is required to tear the film, where σ is the tensile strength of alumina. In total, $F = F_1 + F_2 = b(2\gamma + \sigma(d_i+d_o))$. Reasonable estimates are $\gamma \approx 1$ N/m, $\sigma \approx 100$ MPa. Using d_i =30 nm and d_o = 92 nm [12] we obtain $F_2 \approx 4.6\ F_1$, and therefore the mechanical effect of the alumina layers has to be taken into account As the real structure of the alumina layer is unkown – it could easily consist of a shell structure of a lower strength – this is just a very rough estimate, but it demonstrates that oxidation can significantly increase the forces needed to stretch liquid metallic films exposed to oxygen and to expand a foam. As in a foam the inner cell walls are not oxidised during foaming, the effective increase in force is an average of the outer and interior cell walls and the average force clearly will depend on the size of the foam. Small samples will be more affected by air than large ones as pointed out previously.

The higher rigidity of the oxidised outer skin of an expanding foam can also be seen in Figure 3. When foamed under argon, bubbles can maintain a round shape and protrude into the gas phase. Creation of the oxidised zone suppresses such “surface bubbles”

The thick cell walls observed in the foams indicate a reduced cell wall stabilization because during thinning films rupture earlier. Such thick cell walls are typical for pure aluminium where the minimum cell wall thickness usually ranges from 100 to 120 µm, whereas casting alloys have thinner cell walls, usually 40 µm to 80 µm thick [3]. Some of the cell walls in this study are even thicker, possibly due to the small sample size. The exact reason for different cell wall thicknesses observed in different foams is not yet known.

5 Conclusions

It was shown that

- Aluminium 99.95% foam blown with TiH_2 contains oxides inherited from the oxides already present in the atomised starting powder. These oxides stabilise the cellular structure. The aluminium oxide phases were identified by SAED.
- Oxides form a complex hierarchical structure. The building block are 10 nm large crystallites which cluster together to units of a few 100 nm size, which in turn are found in larger clusters centred around sub-µm sized pores. Such clusters (or metaparticles) can be seen as the elements of the network particles postulated by Körner et al. [8].
- The clusters are irregular in shape and rather loosely connected with each other with large oxide-free areas adjacent to individual clusters.
- Two types of oxides can be postulated: oxides freely floating in the melt and oxides clustered together in plane features along the former powder boundaries.
- A strong correlation between micropores and oxides indicates that such pores are already present in the compacted powder and are then incorporated into the oxide agglomerates after foaming. The oxide clusters are therefore porous.
- Additional oxide is created in a 100 µm thick zone whenever foaming is conducted in air. These additional oxides retard foaming. This can be explained by mechanical forces created by the outer oxide layer grown in the presence of oxygen.
- Unlike freely floating particles which stabilise other types of aluminium foam by surface segregation, the oxides in the foams studies here act in the bulk of the liquid metal films.

Figure 12 sumarises some of the findings of this work and combines them with information from the literature: during foaming in air an additional oxide-rich zone is created which is covered by a thin dense oxide cap layer. Metallic films created in non-oxidising atmospheres contain fewer oxides and are covered by an even thinner oxide cap.

A question which remains open is that of the large-scale structure and configuration of the oxide particles which cannot be analysed by FIB in 3D since the films are too thick. One would like to learn more about the connectivity of the oxide features detected to derive information about the mechanism of stabilisation.

Acknowledments

This work was supported by the German Academic Exchange Service (DAAD) via a scholar stay of A. Dudka at HMI, the ESA-MAP-Program AO-99-075 and the DFG, grant Ba1170 3-3. We thank Oliver Görke for his help with particle size and oxygen content analysis.

References

[1] M.F. Ashby, A.G. Evans, N.A. Fleck, L.J. Gibson, J.W. Hutchinson, H.N.G. Wadley, *Metal Foams – A Design Guide*, Butterworth-Heinemann, Boston (2000)

[2] J. Banhart, Prog. Mater. Sci. 2001;46:559–632

[3] J. Banhart, Adv. Eng. Mater. 2006;8:781–794

[4] M. Weber, *Herstellung von Metallschaum und Beschreibung der Werkstoffeigenschaften, [Manufacture of Metal Foams and Description of Material's Properties]*, Thesis, Universität Bremen, (1995)

[5] J. Banhart, J. Metals 2000;52:22–27

[6] S. Asavavisithchai, A.R. Kennedy, Adv. Eng. Mater. 2006;8:568–572

[7] S. Asavavisithchai, A.R. Kennedy, J. Colloid Interface Sci. 2006;297: 715–723

[8] C. Körner, M. Arnold, R.F. Singer, Mat. Sci. Engnr. A 2005;396:28–40

[9] V. Gergely and T.W. Clyne, Acta Mater. 2004;52:3047–3058

[10] G. Kaptay, In J. Banhart, N.A. Fleck, A. Mortensen, editors, Cellular Metals. Manufacture, Properties, Applications, pp. 107–112. Verlag MIT Publishing, Berlin 2003.

[11] G. Kaptay, Coll. Surf. A 2004;230:67–80

[12] P. Weigand, *Untersuchung der Einflußfaktoren auf die pulvermetallurgische Herstellung von Aluminiumschaum* [*Investigation of the influence of manufacturing parameters on the powder metallurgical preparation of aluminium foam*], Thesis, University of Aachen (1999)

[13] T. Wübben, *Zur Stabilität flüssiger Metallschäume [Stability of liquid metallic foams]*, Thesis, University of Bremen (2004)

[14] F. García-Moreno, A. Rack. L. Helfen, T. Baumbach, S. Zabler, N. Babcsán, J. Banhart, T. Martin, C. Ponchut, M. Di Michiel, Appl. Phys. Lett. 2008;92:134101

[15] F. Simančík, K. Behulová, L. Borš, In J. Banhart, M.F. Ashby, N.A. Fleck, editors, Cellular Metals and Metal Foaming Technology, pp. 89–92, Verlag MIT Publishing, Bremen, 2001.

[16] F. García-Moreno, M. Fromme and J. Banhart, Adv. Eng. Mater. 2004;6:416–420

[17] Ghent University, *Octopus – CT reconstruction software*, http://www.xraylab.com/

[18] H. Zang, Thin Solid Films 1998;320:77–85

[19] ICDD: International Centre for Diffraction Data, http://www.icdd.com/

[20] J. Banhart, H. Stanzick. L. Helfen, T. Baumbach, Appl. Phys. Lett. 2001;78:1152–1154

[21] I. Duarte, J. Banhart, Acta Mater. 2000; 48:2349–2362

[22] P. Schäffler, G. Hanko, H. Mitterer, P. Zach, Porous Metals and Metallic Foams, Proc. Metfoam2007 Conf., Montréal, Sept. 5-7 2007, DEStech Publications, Inc., Pennsylvania, USA, L.P. Lefebvre, J. Banhart, D. Dunand eds., 2008, pp.7–10

[23] S.W. Ip, Y. Wang, J.M. Toguri, Canadian Metallurgy Quarterly 1999;38:81–92

[24] A. Haibel, A. Rack, J. Banhart, Appl. Phys. Lett. 2006;89:154102(1–3)

[25] K. Wefers, C. Misra, *Oxides and hydroxides of aluminum*, Technical Report No. 19, Alcoa Laboratories (1987)

[26] B.C. Lippens, J.H. de Boer, Acta Cryst. 1964;17:1312–1321

[27] G. Bohme, *Non-Newtonian fluid mechanics*, North-Holland, Amsterdam (1987)

[28] S. Freti, J.-D. Bornand, K. Buxmann, Light Metal Age 1982(6); 12–16

[29] F. García-Moreno, N. Babcsán, J. Banhart, Coll. Surf. A 2005;263:290–294

Figures

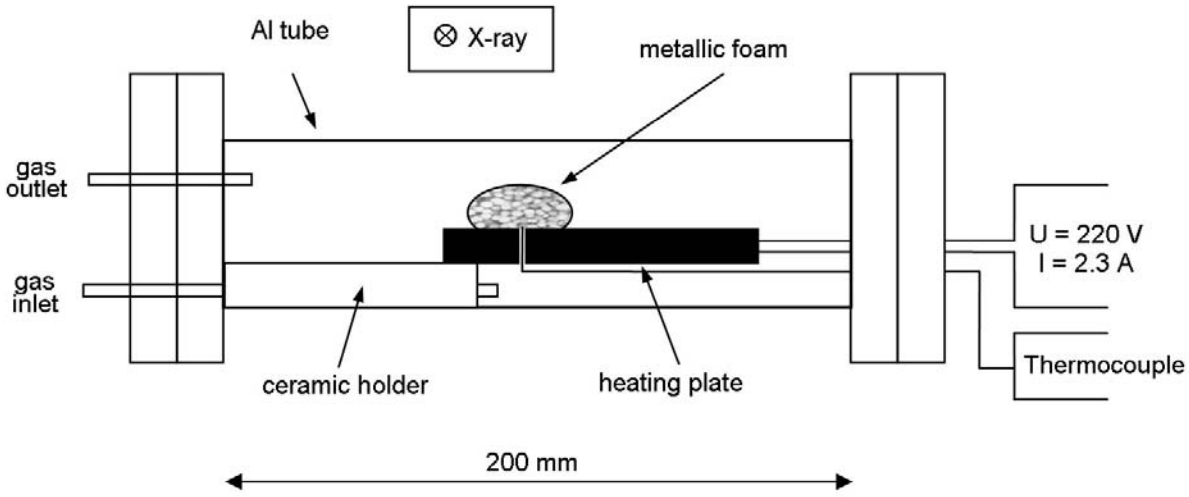

Figure 1. Sketch of furnace used for foaming.

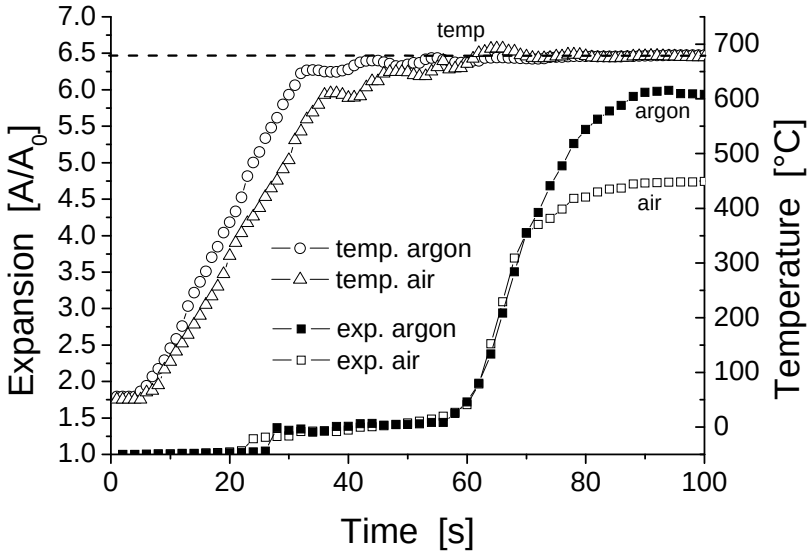

Figure 2. Expansion behaviour of Al99.95 specimens foamed under air and argon. The temperature profile shows two stages: a heating ramp with 18 to 22 K/s for ~30 s, after which the temperature converged to a constant value ~680°C (broken line) during the following 70 s. Expansion is expressed by the projected area A of the foams over the original area A_0.

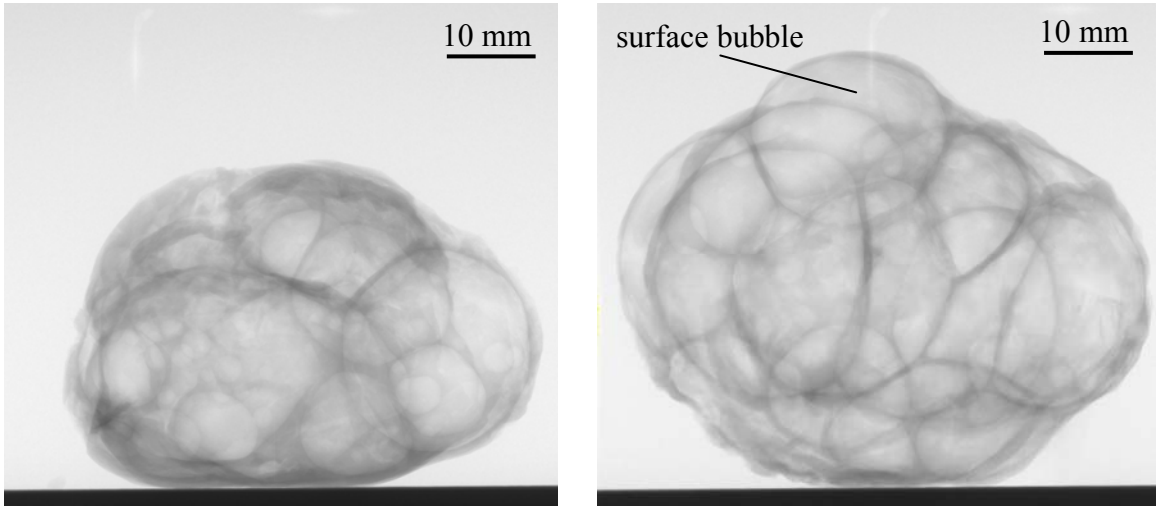

(a) (b)

Figure 3. Radioscopic X-ray images of Al99.95 + 0.5 wt.% TiH_2 foamed under, (a): air and (b): argon. The images were acquired after 100 s of heating (maximum time given in Figure 2).

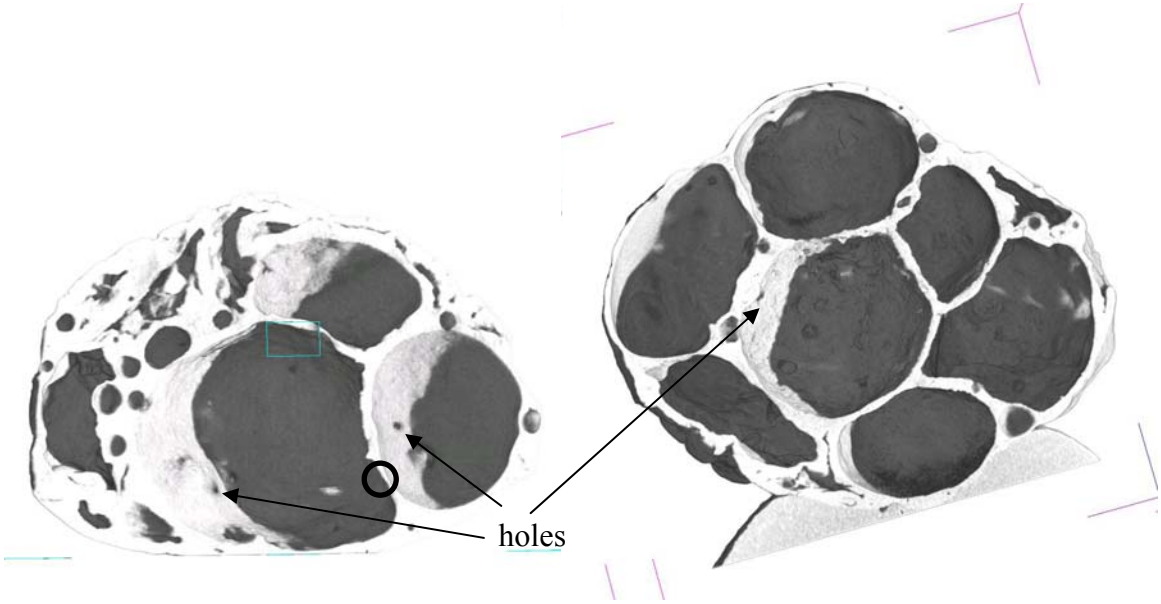

Figure 4. X-ray tomographic reconstruction of the fully expanded Al99.95 samples foamed at T = 680°C, i.e. representing the state shown in Figure 3 after solidification. (a): Foamed in air and (b): under argon. The circle in (a) denotes the position of the sample in Figure 10, the arrows point at holes in cell walls.

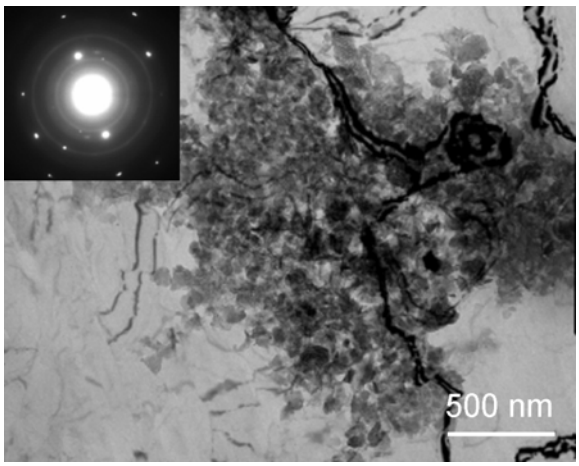

Figure 5. Bright-field TEM micrograph of microtome-sliced aluminium powder particle. Inset: SAED pattern of oxide particles and aluminium matrix.

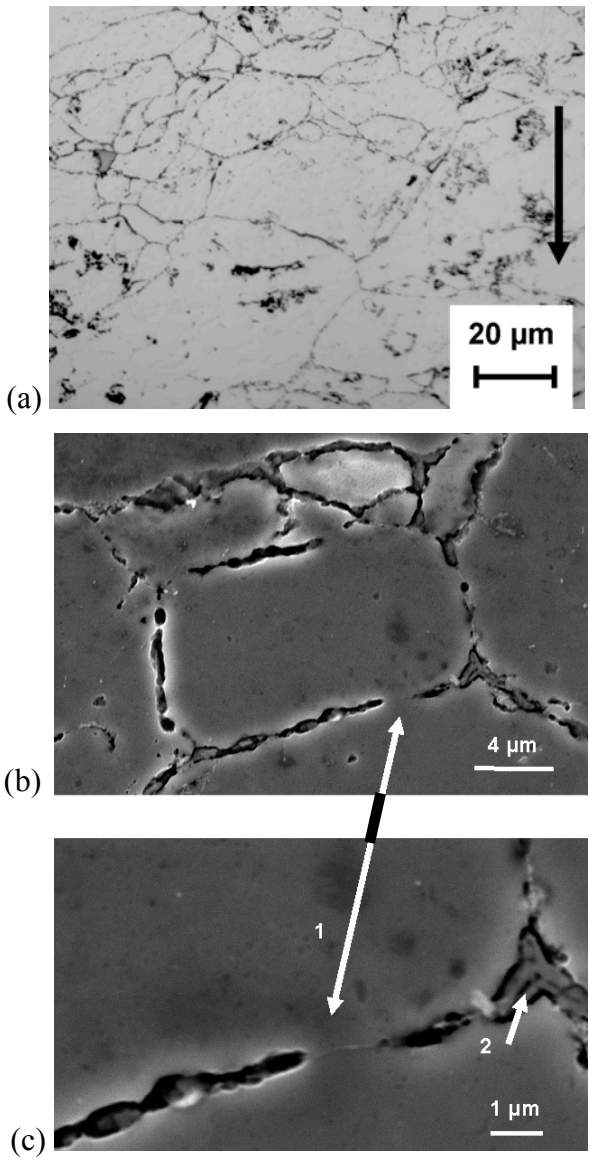

Figure 6. (a) Optical micrograph of the compacted Al-TiH_2 precursor after etching in 98%H_2O + 2%NaOH. The black arrow denotes the pressing direction. (b) SEM image of the same sample. (c) magnification of a particle boundary. Arrow 1 marks metallic bridge between powder particles, arrow 2 an oxide bi-film.

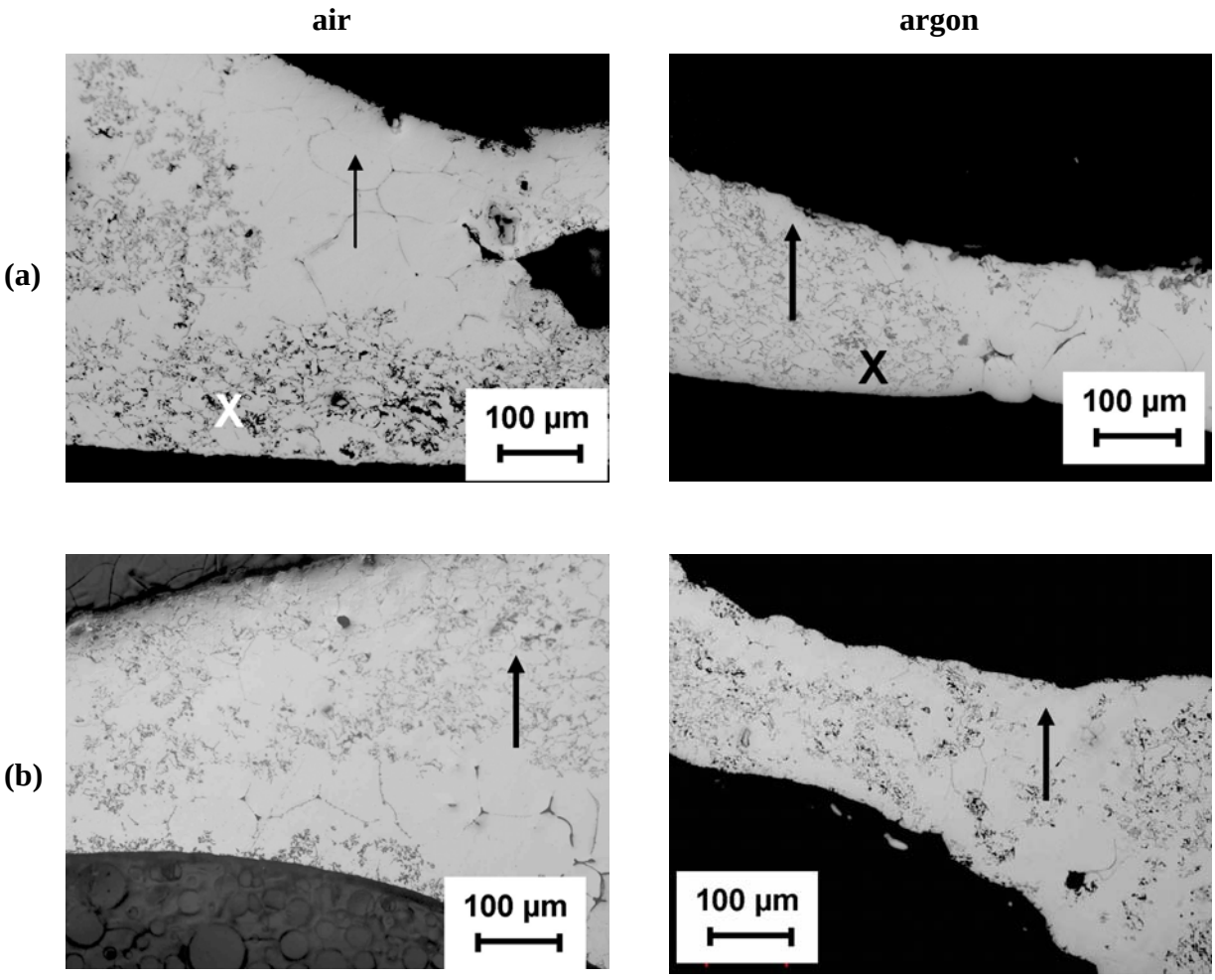

Figure 7. Optical micrographs of different parts of two foams. (a): film at surface of foam, (b): film in the interior of the foam. Two foams are compared: left column: foaming in air, right column: foaming under argon. An "X" in the upper two images denotes the outside of the foam exposed to the ambient gas directly. Arrows point towards the centre of the foam.

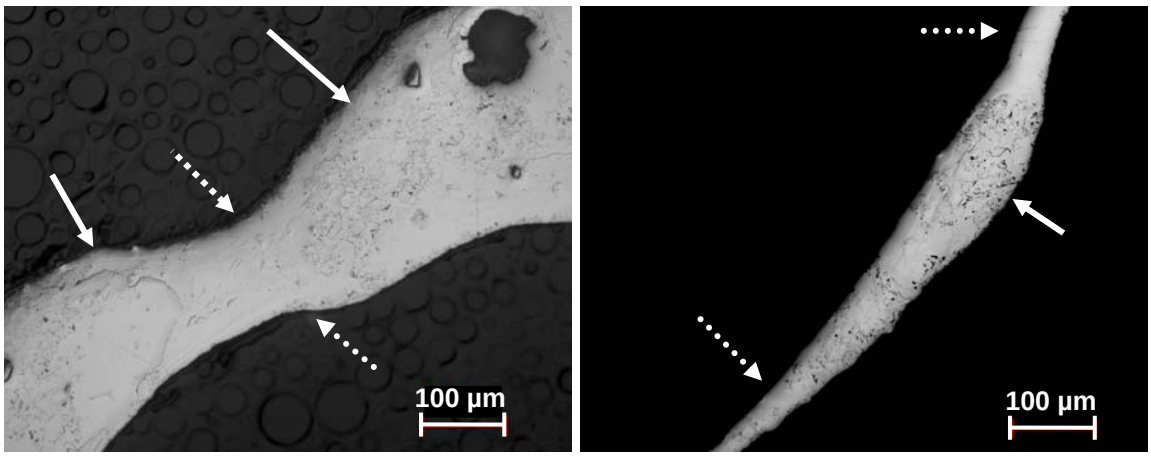

(a) (b)

Figure 8. Optical micrographs of aluminium foam cell walls exhibiting a varying thickness and locally thin sections produced in (a) air and (b) argon. Dotted arrows point at thin and oxide-depleted, full arrows to thick and oxide-containing areas of cell wall.

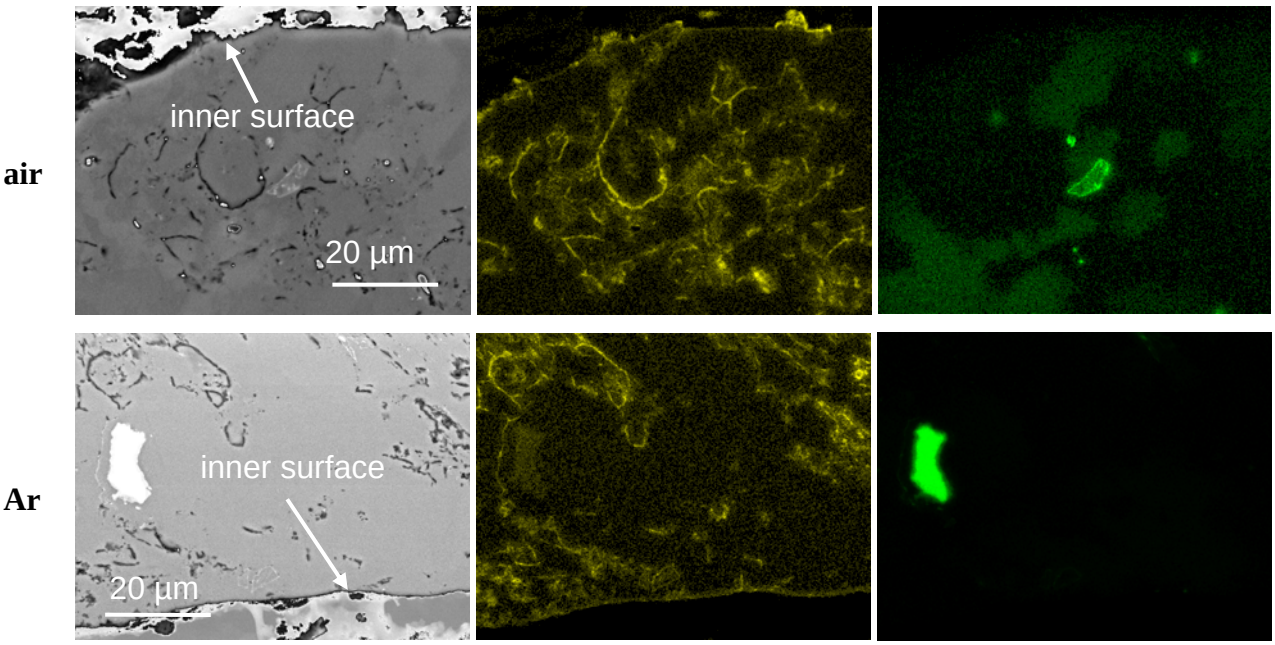

Figure 9. (a) SEM image of an inner cell wall of an aluminium foam produced in air (1st row) or argon (2nd row); (b) and (c) elemental mappings of oxygen and titanium, respectively.

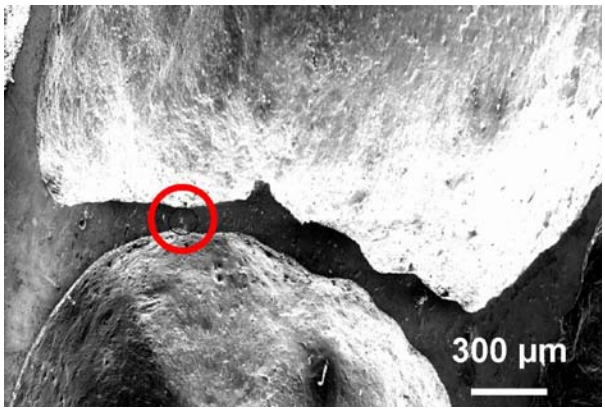

(a)

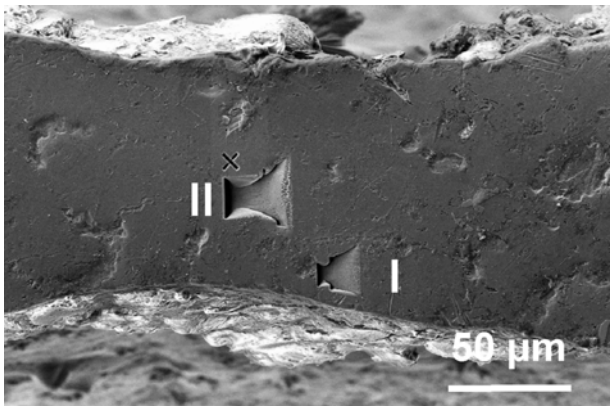

(b)

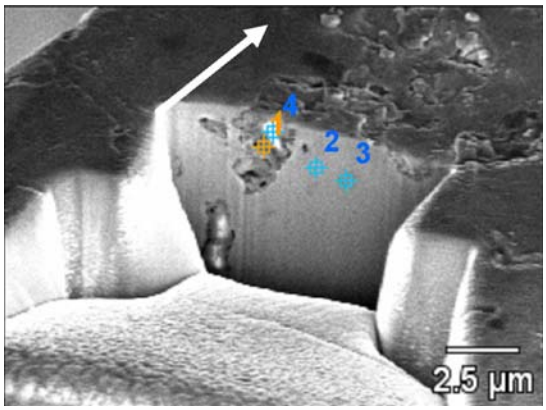

(c)

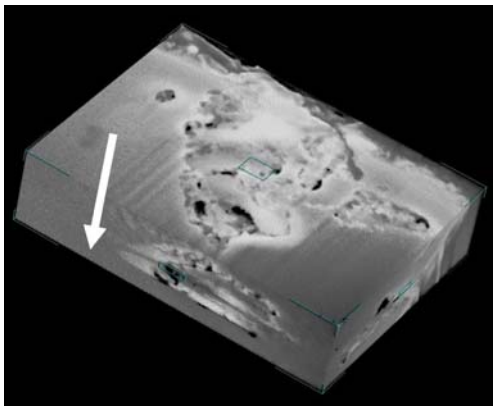

(d)

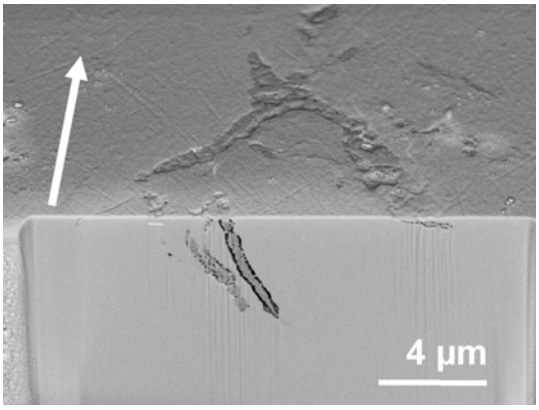

(e)

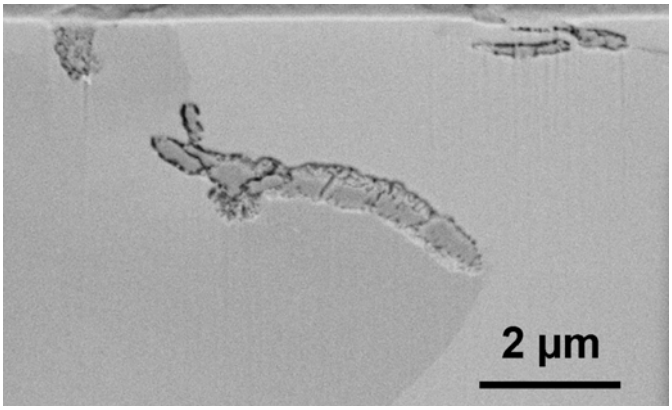

(f)

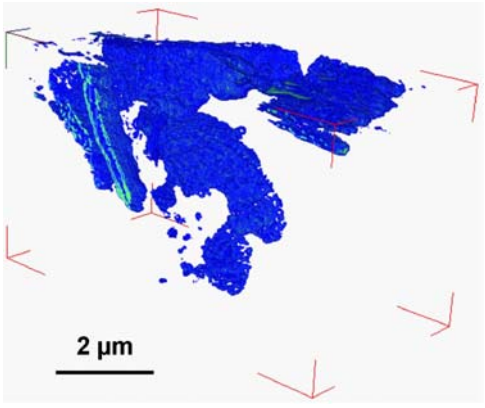

(g)

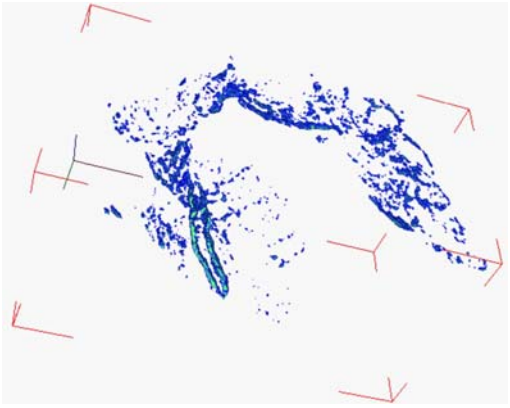

(h)

Figure 10. SEM images of the aluminium foam made in air.

(a) low magnification of cell wall cross section showing the area of interest (circle).

(b) view of the cell wall cross section including the trenches cut by FIB.

(c) side view of trench I showing the area of FIB slicing and markers for the location of EDX analysis. Arrow indicates the direction of FIB slicing.

(d) SEM images of different FIB slices of trench I stacked on top of each other (step width in FIB slicing: 20 nm, total analysed volume: $6\times3.7\times1.2\ \mu m^3$). Arrow indicates the direction of FIB slicing.

(e) side view of trench II, arrow indicates the direction of FIB slicing.

(f) close-up of FIB section in trench II

(g) 3D rendering of alumina in trench II

(h) 3D rendering of pores in trench II

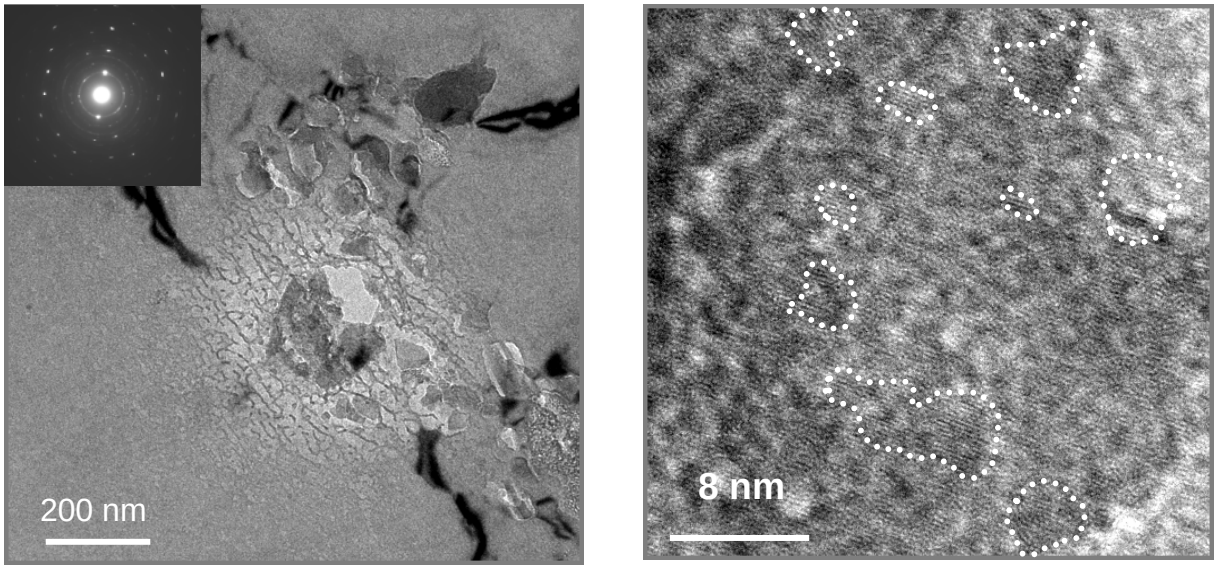

(a) (b)

Figure 11. (a) Bright-field TEM image of foam produced in argon atmosphere; (b) HRTEM image of the oxide particles.

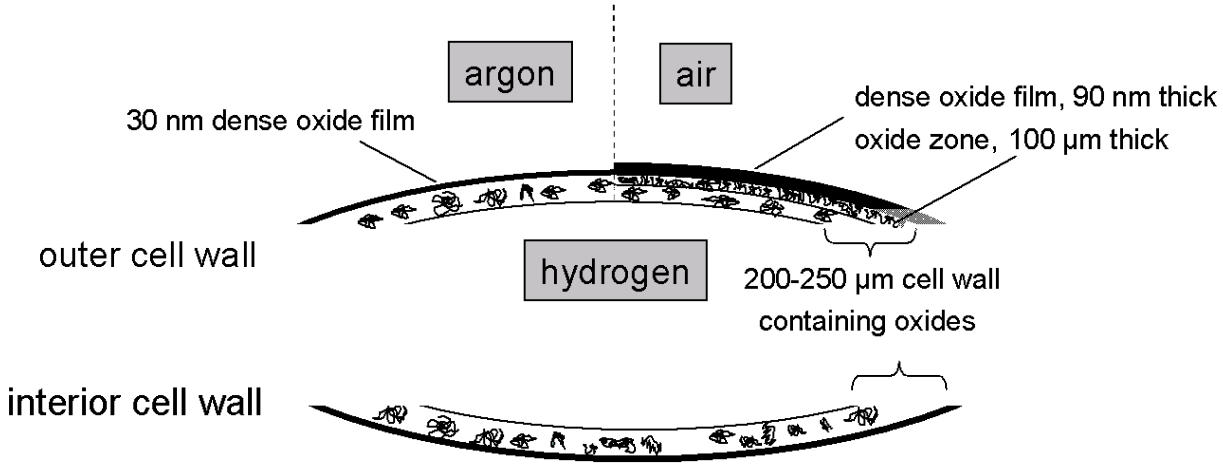

Figure 12. Schematic sketch of the structure of a cell wall in aluminium foam (not to scale).

Table

Table 1. Interplanar spacings d_{exp} in the oxide particles as measured by SAED and compared to the literature.

experimental data			theoretical [19]			
			$Al_{2⅔}O_4$, cubic, a = 0.7906 nm		$Al_{10⅔}O_{16}$, tetragonal, a = 0.56 nm, c = 0.785 nm	
d_{exp}, nm	hkl/cubic	hkl/tetr.	d_{th}, nm	hkl	d_{th}, nm	hkl
			0.456	111	0.456	101
0.402	200	110	0.395	002		
0.283		200			0.280	200
0.278	220		0.279	220	0.278	112
0.238	311	211	0.238	311	0.238	211
0.237		103			0.237	103
0.220	222	202	0.228	222	0.227	202
0.198	400	220	0.197	400	0.198	220
0.196		004			0.196	004
			0.181	331	0.181	301
					0.180	213
			0.177	420		
0.166	422	312	0.161	422	0.161	312
0.152	333	303	0.152	333	0.152	303
0.149	115	105	0.152	115	0.151	105
0.139	044	224	0.140	044	0.139	224